Possible emergence of a skyrmion phase in ferroelectric GaMo_{4}S_{8}

Hui-Min Zhang, Jun Chen, Paolo Barone, Kunihiko Yamauchi, Shuai Dong, and Silvia Picozzi

Possible emergence of a skyrmion phase in ferroelectric $GaMo_4S_8$

Hui-Min Zhang,[1,2] Jun Chen,[1] Paolo Barone,[2] Kunihiko Yamauchi,[3] Shuai Dong,[1,*] Silvia Picozzi[2,†]

[1] *School of physics, Southeast University, Najing 211189, China*

[2] *Consiglio Nazionale delle Ricerche, Institute for Superconducing and Innovative Materials and devices (CNR-SPIN), c/o Univ. "G. D'Annunzio", Chieti 66100, Italy*

[3] *Institute of Scientific and Industrial Research, Osaka University, Ibaraki, Osaka 567-0047, Japan*

Abstract

Polar lacunar spinels, such as GaV_4S_8 and GaV_4Se_8, were proposed to host skyrmion phases under magnetic field. In this work, we put forward, as a candidate for Néel-type skyrmion lattice, the isostructural $GaMo_4S_8$, here systematically studied via both first-principles calculations and Monte Carlo simulations of model Hamiltonian. Electric polarization, driven by Jahn-Teller distortion, is predicted to arise in $GaMo_4S_8$, showing a comparable size but an opposite sign with respect to that evaluated in V-based counterparts and explained in terms of different electron counting arguments and resulting distortions. Interestingly, a larger spin-orbit coupling of $4d$ orbitals with respect to $3d$ orbitals in vanadium-spinels leads to stronger Dzyaloshinskii-Moriya interactions, which are beneficial to stabilize a cycloidal spin texture, as well as smaller-sized skyrmions (radius<10 nm). Furthermore, the possibly large exchange anisotropy of $GaMo_4S_8$ may lead to a ferroelectric-ferromagnetic ground state, as an alternative to the ferroelectric-skyrmionic one, calling for further experimental verification.

* Email: sdong@seu.edu.cn   † Email: silvia.picozzi@spin.cnr.it

I. **Introduction**

Magnetic skyrmions, showing whirl-like spin textures with nontrivial topology, have drawn increasing interests in recent years, due to their appealing potential applications in spintronic devices with low energy consumption [1]. The skyrmion lattice was mostly observed upon application of magnetic fields in metallic alloys with chiral structures, such as FeGe [2], MnGe [3], MnSi [4]. They all share the B20-type crystal structure (space group $P2_13$) [1], a weak magnetocrystalline anisotropy, and common phase diagrams with a helimagnetic ground state. Besides metallic alloys, skyrmions were also found in insulating oxides, such Cu_2OSeO_3, whose space group is $P2_13$ [5-7]. A magnetoelectric coupling is expected in insulating compounds hosting skyrmions, opening up the possibility to manipulate the latter by means of electric field [8].

Magnetic skyrmions can be classified as Bloch-type and Néel-type. When moving from the skyrmion core to the periphery, the spins rotate in a tangential plane (i.e. perpendicular to the radial direction) for Bloch-type skyrmions, whereas they rotate in a radial plane for Néel skyrmions. For the aforementioned chiral magnets, the skyrmions are Bloch-type, which have been extensively investigated. In contrast, the Néel-type skyrmions were predicted to exist in polar materials with the C_{nv} symmetry and then found first in GaV_4S_8 and later in GaV_4Se_8 [9-14]. GaV_4S_8 and GaV_4Se_8 belong to the lacunar spinel AM_4X_8 family (A = Ga and Ge; M = V, Mo; X = S and Se), whose low-temperature structure is rhombohedral (space group $R3m$) with C_{3v} symmetry [15]. In early works, GaV_4S_8 was reported to be a ferromagnet [15-17], but later Nakamura *et al*. showed that GaV_4S_8 is not a simple ferromagnet below T_C since antiferromagnetic signatures (ascribed to spin flips) appears above 5 K [18]. In recent studies, based on atomic force microscopy imaging, complemented with small-angle neutron scattering measurements and theoretical calculations, three magnetic phases were identified in GaV_4S_8: a cycloidal phase, a Néel-type skyrmion lattice phase, and a ferromagnetic phase [12,14,19]. The skyrmion lattice phase in GaV_4S_8 only exists in a very narrow parameter space: temperature ~10-13 K under ~50 mT magnetic field, as reported in Refs. [12,14]. On the other hand, the ground state of GaV_4Se_8 has been reported to display a cycloidal spin phase, implying that the skyrmion lattice can be stabilized in a broader temperature region down to 0 K [13].

Despite being also a member of the lacunar spinel AM_4X_8 family, $GaMo_4S_8$ has been the focus of fewer experimental studies. The very early works claimed it to be ferromagnetic below 19.5 K [20] and a recent theoretical calculation also mentioned ferromagnetism [21]. However, all these studies were done before the discovery of skyrmions in GaV_4S_8, the latter also been erroneously believed to be a simple ferromagnet [12,14]. Therefore, it seems necessary and timely to perform a systematic study, in order to recheck the physical properties of $GaMo_4S_8$. An appealing characteristic of $GaMo_4S_8$, as compared to V-based counterparts, is that the $4d$ orbitals of Mo display larger spin-orbit coupling and more extended spatial distribution than $3d$ orbitals of V, which may result in tuning the subtle

balance between the ferromagnetic, cycloid, and skyrmion phases.

Figure 1(a) shows the minimal unit cell, containing weakly linked molecular units - cubane $(Mo_4S_4)^{5+}$, formed by two interpenetrating Mo_4 and S_4 tetrahedra [see Fig. 1(e)], and tetrahedral $(GaS_4)^{5-}$ as building blocks. According to early experiments, when decreasing the temperature, a structural transition from cubic (F-$43m$, No. 216) to rhombohedral structure ($R3m$, No. 160) occurs at 45.5 K in Ref. [22] and 47 K in Ref. [23], driven by the cooperative Jahn-Teller distortion. At high temperatures, the structure is noncentrosymmetric and nonpolar with the T_d point group, i.e. the Mo-tetrahedron is regular with equivalent Mo ions and Mo-Mo bonds. In the low-temperature polar structure, the Mo-tetrahedron is compressed along the [111] direction, distinguishing the apical (Mo_1) ion from the planar (Mo_2) ions and lowering the symmetry to the C_{3v} point group. Similar Jahn-Teller distortions occur in GaV_4S_8 and GaV_4Se_8 at 38 K [15] and 41 K [13] respectively, but their V-tetrahedra are elongated along the [111] direction, as opposed to the Mo-tetrahedra compression.

II. Methods

Although Ref. [21] briefly mentioned a preliminary density functional theory (DFT) study of $GaMo_4S_8$, a comprehensive investigation is still lacking, especially regarding the possible skyrmion phase. Therefore, in this work, $GaMo_4S_8$ is systematically studied using both DFT and Monte Carlo (MC) simulations based on model Hamiltonian, in order to clarify the similarities and differences between Mo-based and V-based lacunar spinel materials.

The DFT method can deal with electronic structure as well as basic magnetic properties, in small cells (typically with dozens of ions) at zero temperature. However, it can not directly handle the skyrmions at finite temperature and under magnetic fields. Therefore, the model study is necessary, with physical coefficients extracted from the DFT calculations. Generally, MC method can be a powerful tool to determine the thermodynamics phases for a complicated magnetic system. By combining this two methods, it allows us to obtain more comprehensive physics of $GaMo_4S_8$, especially its magnetic properties.

II.A DFT calculation

First-principles DFT calculations were performed using the Vienna *ab initio* Simulation Package (VASP) [24,25] based on the projected augmented wave pseudopotentials. For the exchange-correlation functional, the PBEsol (Perdew-Burke-Ernzerhofrevised for solids) [26] parametrization of the generalized gradient approximation plus U (GGA+U) method [27-29] was used. The Hubbard U_{eff} (=U-J_H, J_H: the Hund exchange) was imposed on Mo's $4d$ orbitals using the Dudarev approach [30] for the structural relaxation, polarization, electronic structure, as well as magnetic ground state without spin-orbit coupling (SOC). We also adopted the Liechtenstein approach, treating separately the U and J_H parameters, [31] to calculate the magnetocrystalline anisotropic energy (MAE) including the anisotropic spin

exchange (ASE) interactions and single ion anisotropy (SIA), as well as Dzyaloshinskii-Moriya (DM) interactions with SOC enabled.

The atomic positions and lattice constants were fully optimized until the Hellman-Feynman forces converged to less than 0.01 eV/Å. The plane-wave cutoff was set to 500 eV. The Monkhorst-Pack k-point meshes were chosen as 7×7×7 in the primitive rhombohedral structure and 6×6×3 in the hexagonal structure. Larger supercells, following the same procedure described in Ref. [32], were used to extract magnetic coefficients. The polarization was calculated by means of both the Berry phase method [33] and Wannier center displacements [34]. The WANNIER90 package was used to obtain the Wannier orbitals of the valence bands [35].

II.B Monte Carlo simulation

The Markov-chain MC method with Metropolis algorithm was employed to simulate the magnetic phase diagram. The MC simulation was done on a $N=36\times36\times3$ hexagonal close-packed lattice with periodic boundary conditions, which was large enough to recover the cycloid phase as well as skyrmions. Larger lattices (e.g. $N=60\times60\times3$) were also verified at some temperature and magnetic field points, confirming the physical results obtained for smaller lattices. For each simulation point, the initial 1×10^5 MC steps were discarded for equilibrium consideration and another 1×10^5 MC steps were retained for statistical averaging of the simulation. The quenching process [36] was used for temperature and magnetic field scanning.

To characterize the magnetic phase transitions, the specific heat C and magnetization M were calculated to determine the critical temperatures [37], which is defined as :

$$C = (<H^2> - <H>^2)/Nk_BT^2 ,$$
(1)

where H is the thermal energy; N is the number of spins; k_B is Boltzmann constant, and T is temperature. For additional insights on the spiral order and skyrmions, the spin structure factors were also calculated. Furthermore, to define the (in-plane) density of skyrmions, the local chirality χ_i was calculated as [4]:

$$\chi_i = [S_i \cdot (S_{i+\hat{x}} \times S_{i+\hat{y}}) + S_i \cdot S_{i-\hat{x}} \times S_{i-\hat{y}})]/8\pi .$$
(2)

In the continuum limit, a single skyrmion gives $\chi = \sum_i \chi_i = 1$.

III. **Results and discussion**

III.A Structural and ferroelectric properties

As a first step, it is necessary to check the basic physical properties of GaMo$_4$S$_8$. For simplicity, the DFT structural relaxation was performed imposing a ferromagnetic spin

configuration. The relaxed lattice constant and rhombohedral angle are shown in Figs. 1(b) and 1(c), respectively, as a function of U_{eff}. These lattice parameters do not show a dramatic dependence on the Hubbard parameter, strengthening the reliability and solidity of our following results. As a reference, in a previous DFT study on GaV_4S_8 an effective Hubbard U-J_H=2 eV was applied on V's $3d$ orbitals [21]. Considering the less localized character of $4d$ orbitals of Mo, as opposed to vanadium $3d$ ones, the Coulomb interactions in $GaMo_4S_8$ are expected to be weaker than in GaV_4S_8. Thus, in the following we will focus on the results obtained with U_{eff}=1 eV, if not otherwise explicitly noted. In the U_{eff}=1 eV case, the discrepancies with respect to experimental values for the lattice constants and rhombohedral angle are small (~-0.45% and ~+0.47% respectively), indicating the reliability of our DFT results.
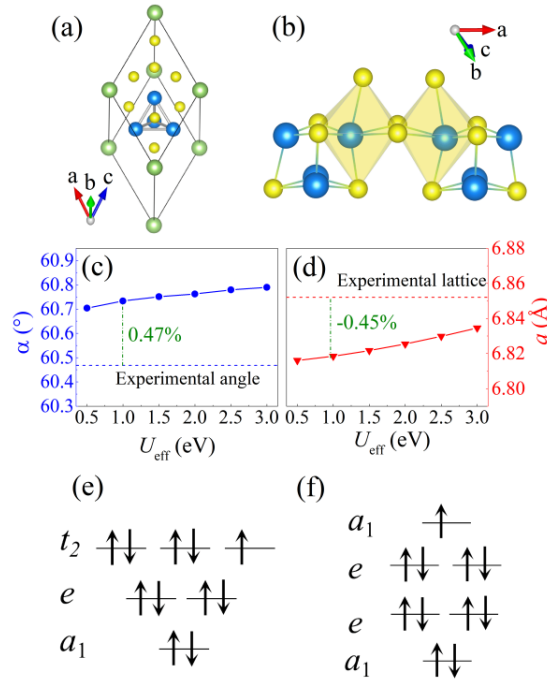

Figure 1. Structure of $GaMo_4S_8$. (a) The low symmetric structure (space group: $R3m$; point group C_{3v}). Green: Ga; Blue: Mo; Yellow: S. The distorted Mo_4 tetrahedron is also shown. (b) Cubane $(Mo_4S_4)^{5+}$ building blocks, highlighting the octahedral coordination of Mo with nearest-neighbour S atoms. (c-d) Optimized lattice constant and angle in the rhombohedral notation as a function of U_{eff}. The experimental values were measured at 8 K [38]. (e-f) The scheme of Mo_4 tetrahedron molecular orbitals arising from symmetry-allowed combinations of atomic t_{2g} orbitals of octahedrally coordinated Mo atoms, with total 11 electrons, as in (e) the high symmetry strucure and (f) the low symmetry structure.

The isostructural (but not isoelectronic) GaV_4S_8 has been reported to display ferroelectricity in its low-temperature structure [12,14], which was later ascribed to a cooperative Jahn-Teller effect, removing an electronic degeneracy by locally elongating V_4

5

tetrahedra along the [111] direction [21]. Since the parent (high-temperature) structure belongs to the noncentrosymmetric T_d point group, the Jahn-Teller distortion carries along an electric polarization, [21,39] which in GaV_4S_8 points towards the apical V_1 atom. The same mechanism is at play also in $GaMo_4S_8$, as sketched in Figs. 2(a-c), the only difference being that the Jahn-Teller effect induces a compression [Fig. 2(c)], rather than an elongation [Fig. 2(b)], of Mo_4 tetrahedra along the [111] direction. As discussed in Refs. [15,21] and in the next section, the opposite Jahn-Teller distortions can be rationalized by taking into account the different number of valence electrons in Mo and V lacunar spinels, leading to different partial filling of the tetrahedral molecular orbitals. As a consequence, the electric polarization in $GaMo_4S_8$ points in the opposite direction as compared to GaV_4S_8, namely from the apical Mo_1 atom to the tetrahedron base, as sketched in Fig. 2(c),

The ferroelectric polarization of $GaMo_4S_8$ is calculated using the Berry phase method, as shown in Fig. 2(d). At variance with what happens for lattice constants and rhombohedral angles, the polarization shows a rather strong dependence on the values of U_{eff}, varying in the range 1.8-0.7 $\mu C/cm^2$. In any case, the existence of polarization is unambiguous and its magnitude is of the order of 1 $\mu C/cm^2$. For U_{eff}=1 eV, the polarization is estimated as ~1.4 $\mu C/cm^2$ (~3.1 $\mu C/cm^2$) using the relaxed (experimental) structure. Thus the polarization seems to be quite sensitive to structural changes, the relaxed structure showing changes in lattice constants below 0.5% and in bond lengths below 1% with respect to the experimental ones. In addition, a very recent work reported a switchable pyroelectric polarization ~0.2-0.4 $\mu C/cm^2$ for $GaMo_4S_8$ polycrystalline samples [23]. Such a value is smaller than our computational estimate, but it becomes in reasonable agreement with our predictions when considering their polycrystalline factor (typically 10%-30% of the single crystalline one). Furthermore, we also calculated the polarization of GaV_4S_8 (~2.55 $\mu C/cm^2$ with U_{eff}=2 eV), that is consistent with the value of 2.43 $\mu C/cm^2$ reported in Ref. [21]. The polarization given by Wannier centers are 1.25 $\mu C/cm^2$ for $GaMo_4S_8$ and 2.00 $\mu C/cm^2$ for GaV_4S_8, in good agreement with the Berry phase method.
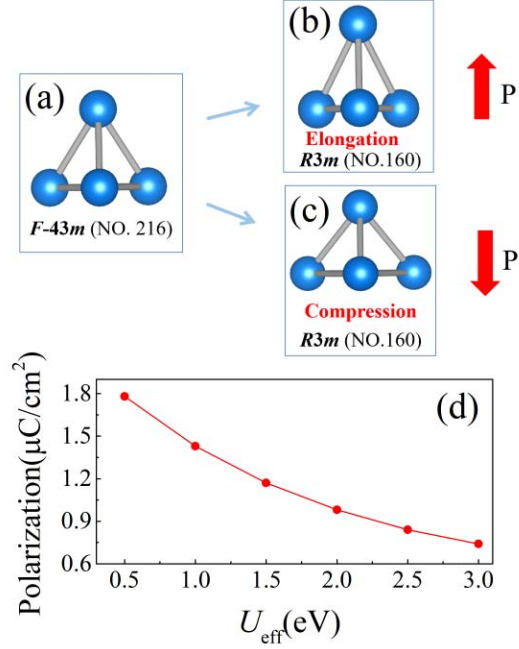
Figure 2. Polarization driven by Jahn-Teller distortion. Four Mo's form a tetrahedron. (a) Mo-tetrahedron in high symmetry (point group T_d) without Jahn-Teller distortion. (b-c) Mo-tetrahedron with Jahn-Teller distortions (elongated/compressed along the [111] direction). The directions of corresponding polarizations are indicated by arrows. In $GaMo_4S_8$, the tetrahedron is compressed. (d) Polarization as a function of U_{eff}.

II.B Band structure and magnetism

To further understand the molecular orbital character of Mo-tetrahedron, the projected band structures are plotted in Figs. 3(a-c). The bandwidths for bands around the Fermi level are quite narrow, since the electronic hopping between Mo-tetrahedra is weak. Thus, each Mo-tetrahedron is similar to a Mo_4 molecular unit. Without SOC, both the highest occupied molecular orbital (HOMO) and lowest unoccupied molecular orbital (LUMO) show the a_1 character. According to the density of states (DOS) (see Fig. 3(d)), there is a small Mott-Hubbard gap of ~0.21 eV, in agreement with previous predictions that gaps are within the range of 0.2~0.3 eV for AM_4X_8 family [40]. When including SOC (a required test due to the presence of heavy 4d element Mo), there is no big change with respect to the scalar relativistic band structure. This shows that SOC does not produce a severe rearrangement of the electronic levels.
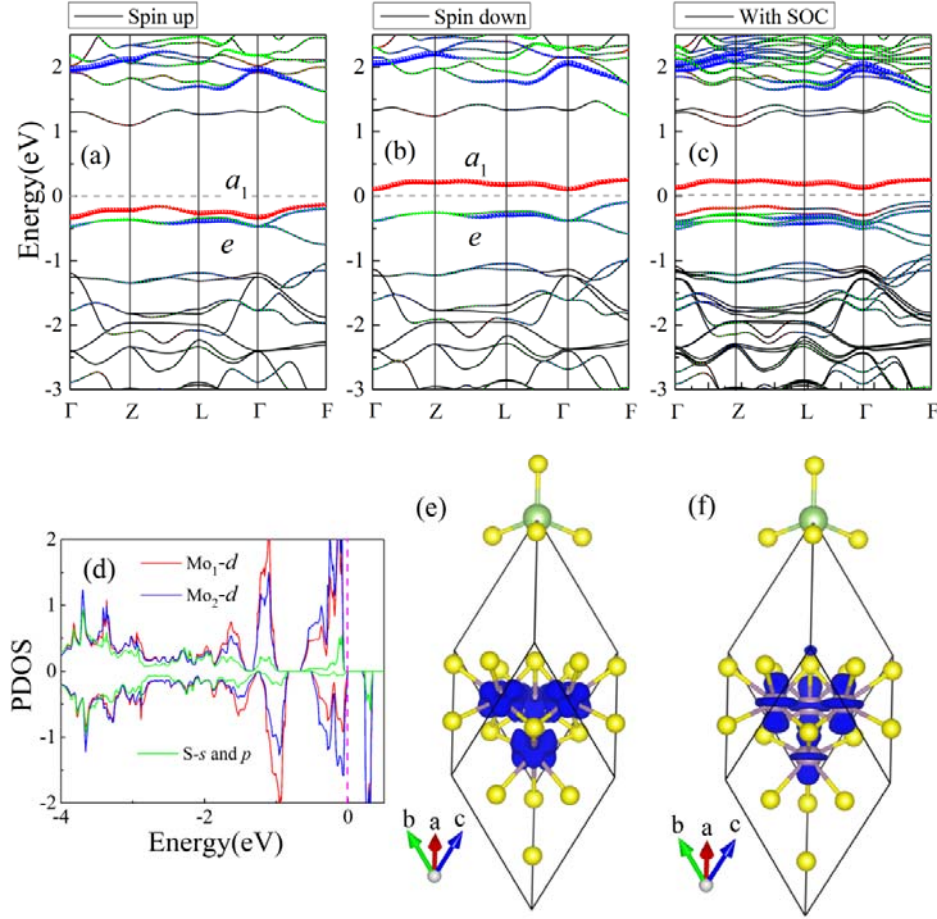
Figure 3. (a-b) Spin-up and spin-down electronic band structures of $GaMo_4S_8$. (c) Electronic band structure with SOC. (d) Atomic PDOS of an apical Mo_1 and a planar Mo_2, and a S with s and p orbitals. The pink dash line represents the Fermi energy. The shapes of (e) e orbital and (f) a_1 orbital from partial density charge calculation.

The electronic structure can be understood from the molecular orbital viewpoint, as sketched in Figs. 1(e-f). Considering the values of Ga^{3+} and S^{2-}, the average valence of Mo is +3.25. Thus the total d electrons for each Mo_4 cluster are 11. In the high symmetric structure, the crystal field of each octahedrally coordinated Mo atom highlighted in Fig. 1(e) splits the atomic orbitals in higher-energy e_g and lower-energy t_{2g} orbitals in the local (octahedral) reference frame. Within each Mo_4 tetrahedron with T_d symmetry, the atomic t_{2g} states form molecular orbitals, with fully occupied a_1, e states and partially occupied three-fold degenerate t_2 states, which are occupied by five electrons, as shown in Fig. 1(e). The partially filled degenerate electronic t_2 state strongly couples to a polar T_2 phonon mode, corresponding to a compression/elongation of the Mo_4 tetrahedral unit which lowers its symmetry from T_d to C_{3v}, and splits into a doubly degenerate e state and a single-degenerate a_1 state. In order to remove the electronic degeneracy,Within each Mo4 tetrahedron the e states are pushed to lower energy and are fully occupied by four electrons, while the single-degenerate a_1 state is

promoted to higher energy (occupied by one electron), as schematically depicted in Fig. 1(f) and consistently with the band structures displayed in Fig. 3(a)-(c) showing both HOMO and LUMO states with a_1 character. The very same mechanism has been discussed for GaV_4S_8 [21], where, however, the molecular orbitals are occupied by seven electrons, which leaves a single electron in the three-fold degenerate t_2 state. In order to remove the degeneracy, the Jahn-Teller distortion of V_4 tetrahedron promotes the e states to higher energy, thus leaving the single electron in the a_1 state which is now pushed to lower energy, opposite to $GaMo_4S_8$. This different behavior can be rationalized taking into account that, in the rhombohedral reference frame, where the z axis is parallel to the [111] polar direction, the a_1 state has a predominant d_{z^2} character. As a consequence, the a_1 state can be pushed to higher (lower) energy by a compression (elongation) of the transition-metal tetrahedral unit along the z axis. [15,21].

In both cases, the presence of an unpaired spin in the valence manifold results in a total magnetization of 1 μ_B per transition-metal tetrahedron.
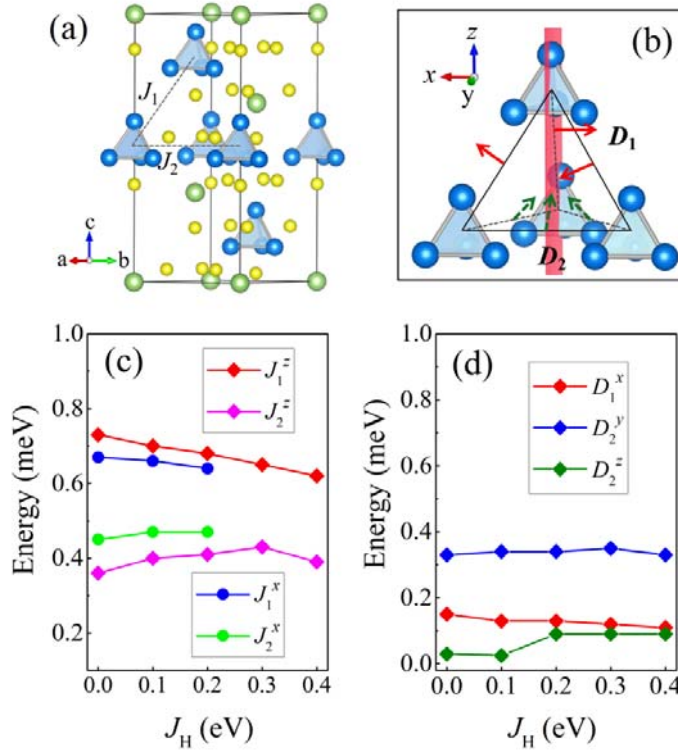

Figure 4. (a) Structure of $GaMo_4S_8$ in the hexagonal setting. The exchange interactions are marked as J_1 (inter-plane) and J_2 (intra-plane). (b) The DM vectors denoted as D_1 (inter-plane) in red and D_2 (intra-plane) in green. The vector directions are determined by the local symmetries: $D_1=(D_1^x, 0, 0)$; $D_2=(0, D_2^y, D_2^z)$. Note that the directions of D_1 and D_2 for each bond will rotate with the bond vector, according to crystal symmetries with triple rotational symmetry. (c-d) Magnetic coefficients as a function of J_H, while U-J_H is fixed to 1 eV. (c) J's with magnetic moments pointing to the z axis and (d) the components of D's.

According to Ref. [32], the magnetic moments in GaV_4S_8 are mainly located on the apical V_1 ion, while the planar V_2 ions only contribute a little spin density. This disproportionation of magnetic moments usually occurs when accompanied by charge ordering, driven by the strong Hubbard repulsion. The situation is quite different in $GaMo_4S_8$. Our DFT calculation suggests that the magnetic moments are in the range 0.21-0.25 μ_B for Mo_1 and all Mo_2's, implying quite homogeneous spin density within the Mo-tetrahedron. The atomic projected DOS (PDOS) also shows the very similar result for Mo_1 and Mo_2 (see Figs. 3(d)). Furthermore, the spatial distributions of partial density charge also confirm the homogeneous a_1 and e molecular orbitals (Figs. 3(e-f)). The distinct character of $GaMo_4S_8$ can be attributed to the more spatial-extended $4d$ orbitals of Mo, which is beneficial to form orbital hybridization within tetrahedron.

Based on the DFT results, a classical spin Heisenberg model is constructed to model the magnetic properties of $GaMo_4S_8$. Taking each Mo-tetrahedron as a magnetic unit, there are two types of bonds between different tetrahedra, with distances 6.82 Å out-of-plane and 6.90 Å in-plane. As shown in Fig. 4(a), the out-of-plane nearest exchange is marked as J_1, while the in-plane nearest exchange is marked as J_2. Similar notation is also applied to the DM vectors, D_1 and D_2. Since the next-nearest neighbour distances are much larger (with 9.70 Å out-of-plane and 11.95 Å in-plane), the corresponding exchange constants are negligible. Then the model Hamiltonian can be written as:

$$H = H_{ex} + H_{DM} + H_{SIA} + H_{Zeeman}$$

$$H_{ex} = -J_{1x} \sum_{<i,j>} (S_i^x \cdot S_j^x + S_i^y \cdot S_j^y) - J_{2x} \sum_{<i,j>} (S_i^x \cdot S_j^x + S_i^y \cdot S_j^y) - J_{1z} \sum_{<i,j>} S_i^z \cdot S_j^z - J_{2z} \sum_{<i,j>} S_i^z \cdot S_j^z$$

$$H_{DM} = -D_1 \cdot \sum_{<i,j>} S_i \times S_j - D_2 \cdot \sum_{<i,j>} S_i \times S_j$$

$$H_{SIA} = -A \sum_i (S_i^z)^2$$

$$H_{Zeeman} = -h \cdot \sum_{<i>} S_i$$

where S_i represents the Heisenberg spin with unit length on site i. H_{ex} is the symmetric exchange interaction, including a XXZ-type anisotropy where J_{1x} and J_{2x} represent the spins pointing in-plane while J_{1z} and J_{2z} represent spins pointing out of plane. H_{DM} includes the DM interactions both in-plane and out of plane. H_{SIA} is the single-ion anisotropy with coupling constant A. H_{zeeman} is the Zeeman energy due to magnetic field h. It should be noted that our model differs from the Heisenberg XXZ model previously studied for GaV_4S_8 [13,14], which was defined on a two-dimensional triangular lattice (thus neglecting J_1 and D_1 interactions) and did not include the single-ion anisotropy.

In order to estimate the magnetic parameters entering in the model Hamiltonian, we calculated the total energies, including SOC, of several collinear and non-collinear spin configurations (cfr Ref. [32]). The model parameters were then extracted by mapping the DFT total energy to the model shown above. Since the magnetic anisotropic energy (MAE)

depends on the choice of Hund coupling term J_H [41], the Liechtenstein approach [31] was adopted to apply the Hubbard correction, keeping U-J_H=1 eV (the simplified Dudarev approach corresponds to the J_H=0 eV limit.). The estimated exchange-interaction parameters are shown in Fig. 4(c-d), displaying only slight changes as a function of J_H. Both inter-plane and intra-plane symmetric exchange-interactions J_1 and J_2 are ferromagnetic, the former being roughly twice the latter. The estimated anisotropy of the dominant symmetric exchange is J_{1z}/J_{1x} = 1.07. On the contrary, and analogously to GaV$_4$S$_8$ [32], the intra-plane DM interaction D_2 is significantly larger than inter-plane D_1. As expected, here the absolute value of DM vectors are larger than those in GaV$_4$S$_8$ [32], due to the stronger SOC of 4d orbitals.

Table 1. The anisotropic symmetric exchange coefficient and the single-ion anisotropic (SIA) coefficient A used in MC simulations.

	J_{1x} (meV)	J_{2x} (meV)	J_{1z} (meV)	J_{2z} (meV)	A (meV)
J_H=0 eV	0.67	0.45	0.72	0.36	0.17
J_H=0.1 eV	0.66	0.47	0.70	0.40	0.32

III.C Magnetic phase transitions

Based on the Heisenberg spin model and using the aforementioned DFT coefficients, MC simulations are performed to study the magnetism under magnetic field at finite temperatures. Starting from J_H=0, the magnetic ordering is simulated as a function of temperature. As shown in Fig. 5(a), the heat capacity peaks at ~17.5 K, very close to the experimentally reported temperature, 19.5 K, although the magnetization remains small in the whole temperature range. A careful analysis on spin structure factor as well as MC snapshot confirms the non-collinear spiral texture in the *ab* plane of hexagonal lattice as the ground state (see Fig. 6(c)). The wave length of a spiral cycloid is about 21 u.c. (~14.6 nm).

By applying a magnetic field along the *c*-axis (i.e. perpendicular to the spiral plane), the spiral texture transforms to the Néel-type skyrmion lattice (see Fig. 6(d) for example) and finally to a full ferromagnetic state, provided the magnetic field is large enough. The global phase diagram for J_H=0 eV is shown in Fig. 6(a). The typical spin textures of both cycloid and skyrmion phases are also plotted in Fig. 6(c-d), with their corresponding in-plane spin structure factor. In the skyrmion phase of J_H=0 eV, a typical radius (r_{Mo}) of each skyrmion is

estimated to be 6.9 nm, much smaller than most previously reported skyrmions (including the sister compound GaV_4S_8: r_V~11 nm [14]). To our knowledge, only the hexagonal Fe film of one-atomic-layer thickness on the Ir(111) surface shows a smaller size (r_{Ir}~1 nm) Néel-type skyrmions so far [42].

The reason for such a small size skyrmion, i.e. high dense skyrmion lattice, might be the large $|D|/J$ ratio, due to the large SOC of 4d orbitals. In fact, in our calculation D_2/J_{2x} (in-plane) is 0.74 , while D/J of GaV_4S_8 (D is the in-plane DM vector, and $J\perp$ represents the in-plane exchange interaction) in Ref. [14] is only 0.35 which is about half of that in $GaMo_4S_8$. As we known, the size of skyrmion lattice is determined by the competition of DM interaction and exchange J, and in inverse ratio to the the value of D/J. When comparing our MC results with r_{Mo} in Ref. [14], the ratio of r_{Mo}/r_V is 0.64, which is semiquantitatively agree with (but slight larger than) the expectation from D/J. The slight quantitative bias is also reasonable considering the enhanced anisotropy energy (the single-ion A and anisotropic exchanges especially for J_2) in $GaMo_4S_8$. Because the anisotropy will suppress the noncollinear texture as well as skyrmion. Also in Ref. [14], the model is purely on a two-dimensional lattice, without A and J_2. Our model lattice is three-dimensional, with more realistic interactions considered.

When increasing the values of J_H, although the exchange interactions J's and DM vectors don't change much, the SIA sizeably increased with J_H =0.1 eV comparing to J_H =0 eV, as shown in Table 1. We also plot the phase diagram (shown in Fig. 6(b)) with the parameters calculated in the case of J_H =0.1 eV. One therefore observes that the skyrmion phase still appears in a small area, and also in the high temperature range.
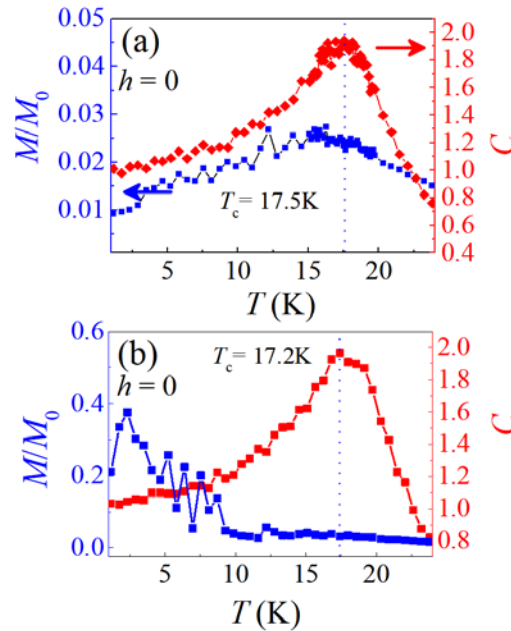
Figure 5. MC results as a function of temperature for (a) $J_H=0$ and (b) $J_H=0.1$ eV. The low magnetization (M) and peak of heat capacity (right axis) suggests non-ferromagnetic (ferromagnetic) ground state for $J_H=0$ ($J_H=0.1$ eV). h denotes the external magnetization field and M_0 denotes the saturated magnetization.
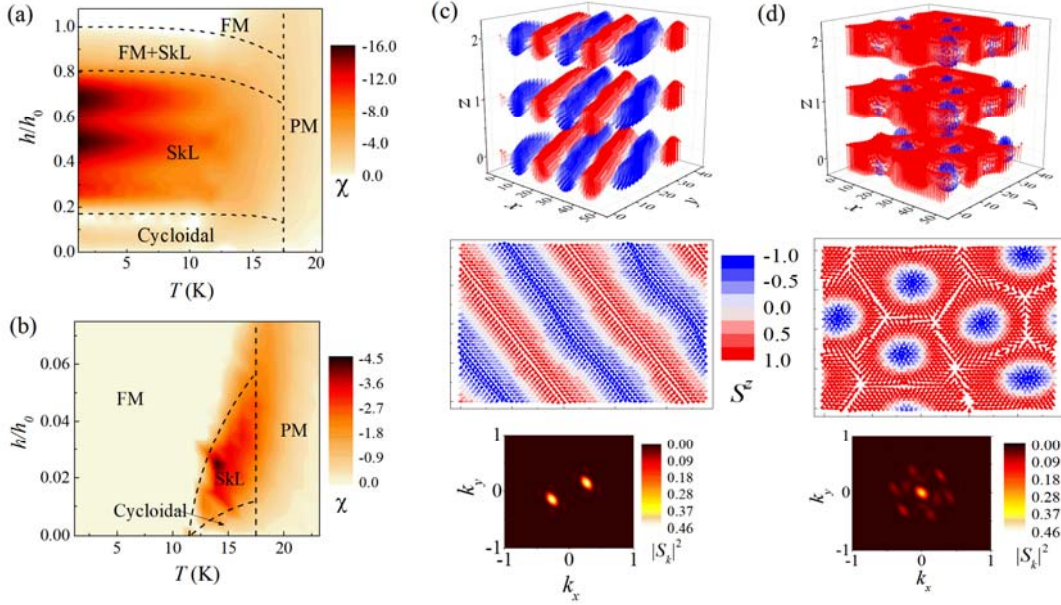

Figure 6. MC phase diagrams for (a) $J_H=0$ eV and (b) $J_H=0.1$ eV. The phase boundaries are determined by heat capacity, magnetic susceptibility, spin structure factors, local spin chirality, as well as snapshots. The peaks of capacity and susceptibility mark the transition points, while the magnetization and local chirality can distinguish different phases, which are further verified by real space snapshots as well as spin structure factors. All these three quantities lead to consistent results. (c) Upper: three-dimensional snapshot of cycloid spin order. Middle: in-plane spin structure factor. Lower: in-plane spin structure factors. (d) Same as (c) but for the skyrmion lattice. The bright points in spin structure factors denote the modulation wave vectors. The double peaks correspond to cycloid spin order while the six-fold peaks reflect the skyrmion lattice. h_0 denotes the saturation magnetization at low temperature.

III.D Comparison with GaV$_4$S$_8$

Finally, it is worth to highlight the differences between GaMo$_4$S$_8$ and GaV$_4$S$_8$, although they are quite similar in structure. First, the different occupation of electrons in d orbitals leads to an opposite sign of polarization upon Jahn-Teller distortions, as found in Sec. III.A and discussed in Sec. III.B. Second, due to the more-extended $4d$ orbitals, the magnetic disproportionation in V-tetrahedrons reported in GaV$_4$S$_8$ [32] is not observed in Mo-tetrahedrons of GaMo$_4$S$_8$. Third, thanks to the larger SOC effect on $4d$ orbitals, the DM interaction in GaMo$_4$S$_8$ is stronger than in GaV$_4$S$_8$. These enhanced DM interactions can lead

to non-collinear spin textures with larger spin angles between nearest neighbors. Thus, the corresponding period of cycloid and size of skyrmions are much smaller in $GaMo_4S_8$, as verified in our MC simulations. However, also due to the larger SOC effect, the MAE may be also larger, which can help the ferromagnetic exchange to stabilize the collinear ferromagnetic ordering, rather than non-collinear ones. For example, the ground state calculated for $J_H=0.1$ eV is ferromagnetic and the skyrmions can only exist in a narrow temperature region just below the Curie temperature. In this sense, the strong SOC is a double-edged sword in pursuing the stabilization of the skyrmion phase in AM_4X_8 spinels.

Although the MAE, resulting from the exchange anisotropy and the SIA, depends to a certain degree on the choice of J_H in DFT calculations, the skyrmion phase can appear with reasonable ASE and SIA values. Therefore, our results suggest that $GaMo_4S_8$ can host high-density skyrmions under magnetic field. However, one should keep in mind that, in case the SIA is experimentally found to be very strong, the ground state could then be ferromagnetic. Even in this case, skyrmions could still be observed with the help of thermal activation, similar to what happens in GaV_4S_8. Nonetheless, both the predicted phases, i.e. ferroelectric-skyrmion or ferroelectric-ferromagnet, are interesting, the results being valuable and undoubtedly calling for further experimental studies.

IV. **Conclusion**

The structural and electronic properties, electric polarization, as well as magnetic interactions in $GaMo_4S_8$ have been systematically studied via DFT simulations. The exchange coupling constants and DM interactions show comparable values, their competition inducing very peculiar magnetic properties. Non-collinear magnetic states were predicted by using the MC approach with model parameters estimated from DFT. Importantly, the skyrmion lattice phase was predicted to probably appear in a large area of the phase diagram, which depends on the intensity of Hund coupling. Despite the similarity between GaV_4S_8 and $GaMo_4S_8$, the peculiarities of $4d$ orbitals (i.e. larger spatial extension as well as stronger SOC) lead to different results, in terms of increased phase stability for the skyrmionic phase and appealing reduced size of the skyrmions. Our predictions are therefore expected to stimulate future experiments, aiming at studying high-density skyrmion lattices in lacunar spinels and related systems.

References

[1] N. Nagaosa and Y. Tokura, Nat. Nanotechnol. **8**, 899 (2013).

[2] X. Z. Yu, N. Kanazawa, Y. Onose, K. Kimoto, W. Z. Zhang, S. Ishiwata, Y. Matsui, and Y. Tokura, Nat. Mater. **10**, 106 (2011).

[3] T. Tanigaki, K. Shibata, N. Kanazawa, X. Z. Yu, Y. Onose, H. S. Park, D. Shindo, and Y. Tokura, Nano Lett. **15**, 5438 (2015).

[4] S. D. Yi, S. Onoda, N. Nagaosa, and J. H. Han, Phys. Rev. B **80**, 054416 (2009).

[5] S. Seki, X. Z. Yu, S. Ishiwata, and Y. Tokura, Science **336**, 198 (2012).

[6] T. Adams, A. Chacon, M. Wagner, A. Bauer, G. Brandl, B. Pedersen, H. Berger, P. Lemmens, and C. Pfleiderer, Phys. Rev. Lett. **108**, 237204 (2012).

[7] S. Seki, J. H. Kim, D. S. Inosov, R. Georgii, B. Keimer, S. Ishiwata, and Y. Tokura, Phys. Rev. B **85**, 220406(R) (2012).

[8] J. S. White, K. Prša, P. Huang, A. A. Omrani, I. Živković, M. Bartkowiak, H. Berger, A. Magrez, J. L. Gavilano, G. Nagy *et al.*, Phys. Rev. Lett. **113**, 107203 (2014).

[9] A. Bocdanov and A. Hubert, Phys. Status Solidi B **186**, 527 (1994).

[10] A. Bogdanov and A. Hubert, J. Magn. Magn. Mater **138**, 255 (1994).

[11] Leonov, A. Twisted, localized, and modulated states described in the phenomenological theory of chiral and nanoscale ferromagnets. PhD thesis (2011); http://nbn-resolving.de/urn:nbn:de:bsz:14-qucosa-83823

[12] E. Ruff, S. Widmann, P. Lunkenheimer, V. Tsurkan, S. Bordács, I. Kézsmárki, and A. Loidl, Sci Adv. **1**, e1500916 (2015).

[13] Y. Fujima, N. Abe, Y. Tokunaga, and T. Arima, Phys. Rev. B **95**, 180410(R) (2017).

[14] I. Kézsmárki, S. Bordács, P. Milde, E. Neuber, L. M. Eng, J. S. White, H. M. Rønnow, C. D. Dewhurst, M. Mochizuki, K. Yanai *et al.*, Nat. Mater. **14**, 1116 (2015).

[15] R. Pocha, D. Johrendt, and R. Pöttgen, Chem. Mater. **12**, 2882 (2000).

[16] Y. Sahoo and A. K. Rastogi, J. Phys. Condens. Matter **5**, 5953 (1993).

[17] H. Müller, W. Kockelmann, and D. Johrendt, Chem. Mater. **18**, 2174 (2006).

15

[18] H. Nakamura, R. Ikeno, G. Motoyama, T. Kohara, Y. Kajinami, and Y. Tabata, J. Phys. Conf. Ser. **145**, 0120770 (2009).

[19] S. Widmann, E. Ruff, A. Günther, H. A. Krug von Nidda, P. Lunkenheimer, V. Tsurkan, S. Bordács, I. Kézsmárki, and A. Loidl, Philos. Mag. **97**, 3428 (2016).

[20] A. K. Rastogi, A. Berton, J. Chaussy, R. Tournier, M. Potel, R. Chevrel, and M. Sergent, J. Low Temp. Phys. **52**, 539 (1983).

[21] K. Xu and H. J. Xiang, Phys. Rev. B **92**, 121112(R) (2015).

[22] H. Barz, Mater. Res. Bull. **8**, 983 (1973).

[23] E. Neuber, P. Milde, A. Butykai, S. Bordacs, H. Nakamura, T. Waki, Y. Tabata, K. Geirhos, P. Lunkenheimer, I. Kézsmárki *et al.*, J. Phys. Condens. Matter **30**, 445402 (2018).

[24] G. Kresse and J. Hafner, Phys. Rev. B **47**, 558 (1993).

[25] G. Kresse and J. Furthmüller, Phys. Rev. B **54**, 11169 (1996).

[26] J. P. Perdew, A. Ruzsinszky, G. I. Csonka, O. A. Vydrov, G. E. Scuseria, L. A. Constantin, X. L. Zhou, and K. Burke, Phys. Rev. Lett. **100**, 136406 (2008).

[27] J. P. Perdew, K. Burke, and M. Ernzerhof, Phys. Rev. Lett. **77**, 3865 (1996).

[28] G. Kresse and D. Joubert, Phys. Rev. B **59**, 1758 (1999).

[29] P. E. Blöchl, Phys. Rev. B **50**, 17953 (1994).

[30] S. L. Dudarev, G. A. Botton, S. Y. Savrasov, C. J. Humphreys, and A. P. Sutton, Phys. Rev. B **57**, 1505 (1998).

[31] A. I. Liechtenstein, V. I. Anisimov, and J. Zaanen, Phys. Rev. B **52**, R5467 (1995).

[32] J. T. Zhang, J. L. Wang, X. Q. Yang, W. S. Xia, X. M. Lu, and J. S. Zhu, Phys. Rev. B **95**, 085136 (2017).

[33] R. Resta, Rev. Mod. Phys. **66**, 899 (1994).

[34] R. D. King-Smith, and D. Vanderbilt, Phys. Rev. B **47**, 1651(R) (1993).

[35] A. A. Mostofi, J. R. Yates, Y.-S. Lee, I. Souza, D. Vanderbilt, and N. Marzari, Comput. Phys. Commun. **178**, 685 (2008).

[36] A. Baumgärtner, K. Binder, A. N. Burkitt, D. M. Ceperley, H. De Raedt, A. M. Ferrenberg, D. W. Heermann, H. J. Herrmann, D. P. Landau, D. Levesque *et al.*, *The Monte Carlo method in condensed matter physics* (Springer Science & Business Media, 2012), Vol. 71

[37] M. Janoschek, M. Garst, A. Bauer, P. Krautscheid, R. Georgii, P. B ni, and C. Pfleiderer, Phys. Rev. B **87**, 134407 (2013).

[38] M. Francois, W. Lengauer, K. Yvon, M. Sergent, M. Potel, P. Gougeon, and H. B. Yaich-Aerrache, Z. Kristallog. Cryst. Mater. **196**, 111 (1991).

[39] P. Barone, K. Yamauchi, and S. Picozzi, Phys. Rev. B **92**, 014116 (2015).

[40] M. Querré, B. Corraze, E. Janod, M. P. Besland, J. Tranchant, M. Potel, S. Cordier, V. Bouquet, M. Guilloux-Viry, L. Cario, Key Eng. Mater. **617**, 135 (2014).

[41] E. Bousquet and N. Spaldin, Phys. Rev. B **82**, 220402(R) (2010).

[42] K. Von Bergmann, S. Heinze, M. Bode, E. Y. Vedmedenko, G. Bihlmayer, S. Blügel, and R. Wiesendanger, Phys. Rev. Lett. **96**, 167203 (2006).